The Swift-XRT imaging performances and serendipitous survey

A. Moretti[a], M. Perri[b], M. Capalbi[b], A.F. Abbey[c], L. Angelini[d], A. Beardmore[c], D.N. Burrows[e], S. Campana[a], G. Chincarini[a,f], O. Citterio[a], G. Cusumano[g], P.A. Evans[c], P. Giommi[b], M.R. Goad[c], O. Godet[c], C. Guidorzi[a,f], D. Grupe[e] J.E. Hill[d], J.A. Kennea[e], V. La Parola[g], V. Mangano[g], T. Mineo[g], D.C. Morris[e], J.A. Nousek[e], J.P. Osborne[c] K.L. Page[c], C. Pagani[e], J. Racusin[e], P. Romano[a,f], G. Tagliaferri[a], F. Tamburelli[b],

[a] INAF-Osservatorio Astronomico di Brera, Via Bianchi 46, 23807 Merate, LC, Italy
[b] ASI-ASDC, Via G. Galilei, I-00044 Frascati, Italy
[c] University of Leicester, University Road, Leicester LE1 7RH, UK
[d] NASA-GSFC, Greenbelt, MD 20771, USA
[e] Pennsylvania State University, 525 Davey Lab, University Park, PA 16802, USA
[g] Università degli Studi di Milano, Bicocca, Piazza delle Scienze 3, I-20126, Milano, Italy
[g] INAF-IASF, Via U. La Malfa 153, 90146 Palermo, Italy

ABSTRACT

We are exploiting the Swift X-ray Telescope (XRT) deepest GRB follow-up observations to study the cosmic X-Ray Background (XRB) population in the 0.2-10 keV energy band. We present some preliminary results of a serendipitous survey performed on 221 fields observed with exposure longer than 10 ks. We show that the XRT is a profitable instrument for surveys and that it is particularly suitable for the search and observation of extended objects like clusters of galaxies. We used the brightest serendipitous sources and the longest observations to test the XRT optics performance and the background characteristics all over the field of view, in different energy bands during the first 2.5 years of fully operational mission.

Keywords: *Swift*, XRT, Survey

1. INTRODUCTION

The *Swift* satellite[1] was successfully launched on 2004 Nov 20. The scientific payload includes one wide-field instrument, the gamma-ray Burst Alert Telescope (BAT[2]), and two narrow-field instruments, the X-Ray Telescope (XRT[3]), and the Ultraviolet/Optical Telescope (UVOT[4]). The XRT is an X-ray CCD imaging spectrometer. It utilizes the third flight mirror module (FM3) originally developed for the JET–X program: it consists of 12 nested, confocal and coaxial mirror shells having a Wolter I configuration. The mirror diameters range from 191 mm to 300 mm, the nominal focal length is 3500 mm, the total field of view is about 40 arcminutes (at 50% vignetting level) and the effective area at 1.5 keV is $\sim$ 120 cm^2(mirror plus filter and CCD quantum efficiency). The XRT imaging array is a e2v technologies CCD22 consisting of 600 x 600 pixels, each 40μm $\times$40μm, with a nominal plate scale of 2.36 arcseconds per pixel, which makes the effective field of view of the system $\sim$ 24 arcmin.[3]

The XRT was designed to measure the position, flux, spectrum, and light curve of GRB afterglows over a wide flux range covering more than seven orders of magnitude in flux in the energy band 0.2–10 keV. It has been performing extraordinary and unprecedented observations of the early phases of the gamma-ray burst afterglows. Here we intend to show that XRT is also a profitable instrument for surveys and that it is particularly suitable for the search and observation of extended objects like clusters of galaxies. In this paper we use photon counting mode data with the standard grade selection, grade 0-12, reduced by means of the *xrtpipeline* task of the current release of the HEADAS software (version 6.3.1).

Correspondence to alberto.moretti@brera.inaf.it, INAF-Osservatorio Astronomico di Brera, Via Bianchi 46, 23807 Merate, LC, Italy

Optics for EUV, X-Ray, and Gamma-Ray Astronomy III, edited by Stephen L. O'Dell, Giovanni Pareschi
Proc. of SPIE Vol. 6688, 66880G, (2007) · 0277-786X/07/$18 · doi: 10.1117/12.734087

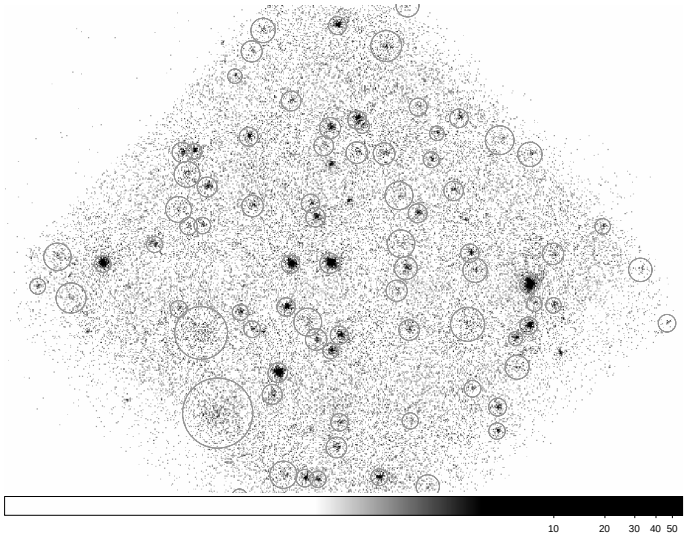

Figure 1. We show the 416 ks follow–up observation of GRB051221. The detection is performed by means of a wavelet detection algorithm. Two galaxy clusters are visible in the left-bottom angle of the field of view.

The outline of the paper is the following. In Section 2 we present the general characteristics of the deep fields serendipitous survey. In Section 3 we use the brightest serendipitous sources to test the imaging performance (PSF, HEW and position accuracy) all over the field of view and in different energy bands. In Section 4 using the deepest exposure we present the background timing and spectral characteristics. In Sections 5 and 6 we present in detail the flux limits of point–like and extended sources.

2. THE SERENDIPITOUS SURVEY

We used all the GRB follow-up observations performed by the XRT since the start of the mission up to June 2007 and with nominal exposure time longer than 10 ks (Fig. 1). This consists of 221 observations with a total exposure time of 2.6×10^7 seconds which is equivalent to 298 days, i.e. 33% of the total elapsed time since the beginning of the mission (Fig. 2). We applied the Brera Multiscale Wavelet (BMW) detection algorithm on the 221 fields ($\sim$25 nominal square degrees) to produce a photometric catalog of sources in 4 (overlapping) energy bands: 0.3-10, 0.5-2, 2-10, 5-10 keV. The BMW detection algorithm is based on a wavelet transform algorithm and it has already been successfully applied to ROSAT-HRI and Chandra images[5,6,7].[8] The catalog consists of 7151 sources, with 315 having more than 300 counts. 5128 sources have absolute galactic latitude higher than 20 degrees and, among them, 84 can be classified as extended with 4σ significance (see below).

3. THE IMAGING PERFORMANCE

3.1. Point Spread Function (PSF) And Half Energy Width (HEW)

We used the highest fluence sources (with more than 1000 counts) to study the PSF dependence on energy and off–axis angle and to test the current status of the calibrations.

The in–flight PSF calibration consisted of some observations of faint point–like sources with different spectral properties.[9] These were performed in different positions of the detector in order to observe the surface brightness (SB) profile as a function of the energy (E) and the distance from the optical axis of the telescope. The final product of the in–flight calibration was an analytical model that reproduces the SB profile of a generic point–like source and can be used for the calculation of the PSF corrections. As shown in[9] the PSF can be analytically described by a King function:

$$\mathrm{PSF(r)} = (1 + (\frac{\mathrm{r}}{\mathrm{r_c(E,\theta)}})^2)^{-\beta(\mathrm{E},\theta)} \quad (1)$$

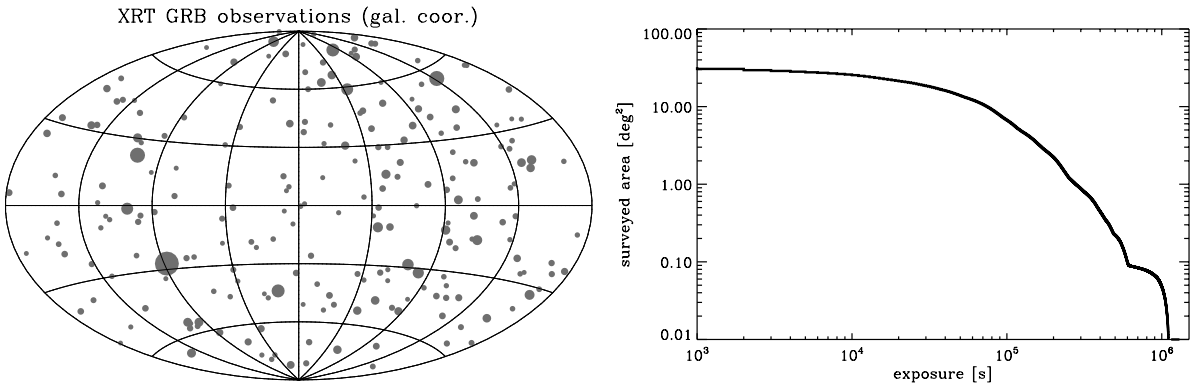

Figure 2. Left panel: the galactic coordinates of the 221 deep fields. The dimension of the circles are proportional to the exposure times. **Right Panel:** the survey sky–coverage in terms of exposure time.

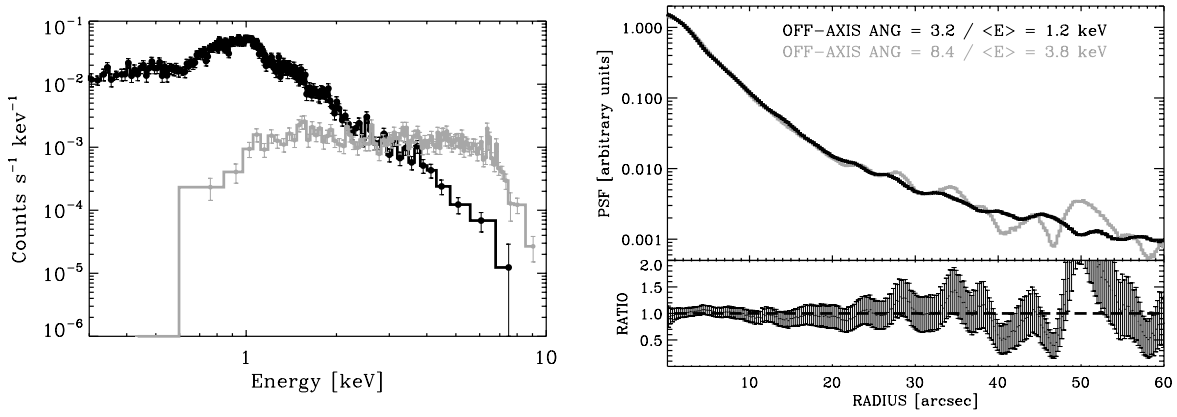

Figure 3. Left panel: The spectra of two different high fluence sources with mean energy of 1.2 and 3.8 keV respectively.**Right panel:** The PSF of the two sources are very similar with ratio residuals at level of $< 5\%$, although they have completely different spectra and are observed in different positions of the field of view.

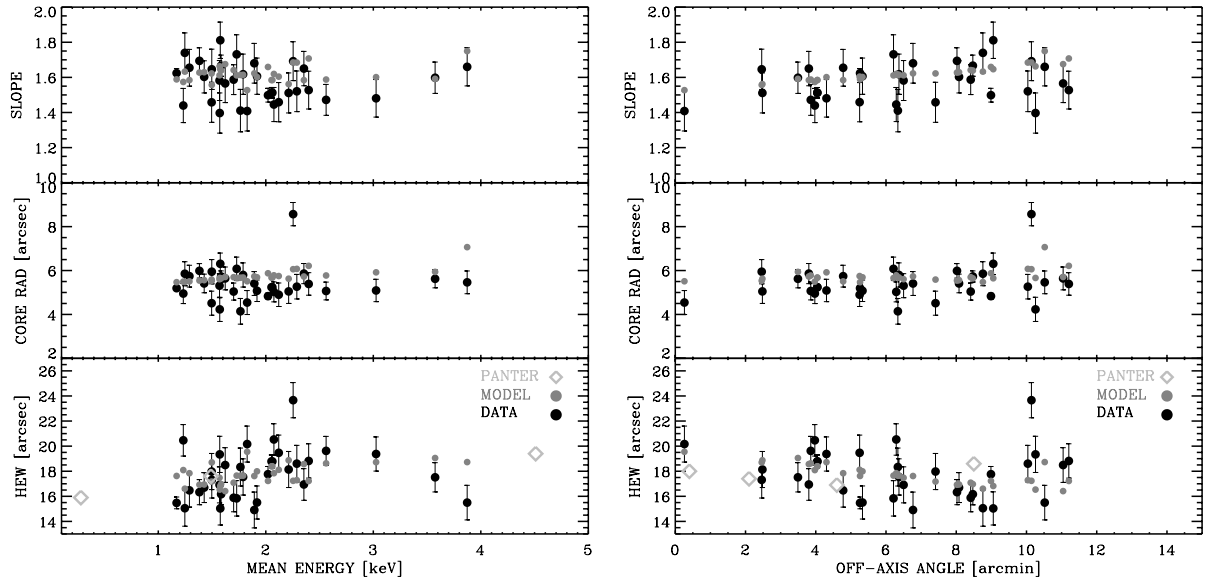

Figure 4. Left panel: The PSF dependence on energy. For a sample of high fluence serendipitous sources we show the core radius values (central panel), the slope (upper panel) and the HEW (bottom panel). **Right panels**: the same values plotted as a function of the off-axis angle.

This model has 2 free parameters (plus the normalization), the core radius (r_c) and the slope (β) which are functions of the energy E and the distance from the optical axis θ.

$$\mathrm{r_c(E,\theta) = a_1 + b_1 \times \theta + c_1 \times E + d_1 \times E \times \theta} \quad (2)$$

$$\beta(E,\theta) = a_2 + b_2 \times \theta + c_2 \times E + d_2 \times E \times \theta \quad (3)$$

The values of the plane function coefficients are stored in the PSF file within the *Swift* XRT CALDB distribution (http://swift.gsfc.nasa.gov/docs/swift/analysis). In this way, given the position within the field of view and the energy for a hypothetical monochromatic source we can calculate the corresponding values of r_c and β and reproduce the PSF by means of this parametrization. As pointed out by[9] the PSF dependence on the off–axis angle is very weak. This is due to the fact that the CCD is intentionally slightly offset along the optical axis from the best on–axis focus in order to have a uniform PSF over a large fraction of the field of view. On the other hand, if we consider the whole energy band PSF, the energy dependence is also very weak; this is simply due to the fact that, usually, the overall PSF is mostly determined by photons with energy lower than 2 keV.

Here we used 34 high fluence sources detected in the serendipitous survey to test the PSF calibration on the largest possible range of energies and off–axis angle. As an example, in Fig. 3, we compare the profiles of two sources, with completely different spectrum (mean energy 1.2 and 3.8 keV respectively) and observed in very different positions of the telescope field of view (3.3 and 8.4 arcmin off–axis angle respectively): their PSFs present negligible differences ($< 5\%$).

In Fig.4 we plot the HEW values (diameter that contains 50% of the total flux), the PSF core radius (r_c) and the slope (β) of the 34 high fluence serendipitous sources as a function of the mean energy of the spectrum and the off–axis angle.

3.2. Positional accuracy and boresight drift

From the serendipitous catalog we selected sources with more than 200 counts and with positions measured by optical catalogs with < 1 arcsec precision. We used them, together with some pointed sources and some GRB afterglows to test the XRT position accuracy.

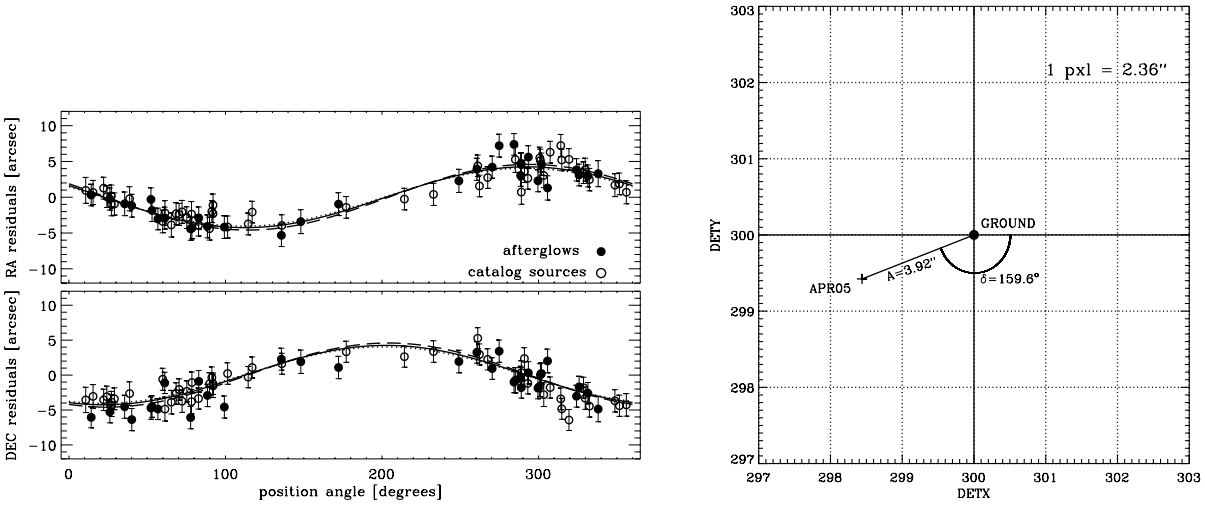

Figure 5. Left panel: a small misalignment between the XRT and the star tracker produces a trigonometric relationship between the spacecraft position angle of the observations and the residuals in RA and DEC of the X–ray positions in respect to the optical positions. **Right panel:** The amplitude of the trigonometric function is the amplitude A of the misalignment and the phase δ is the direction on the CCD detector coordinates frame.

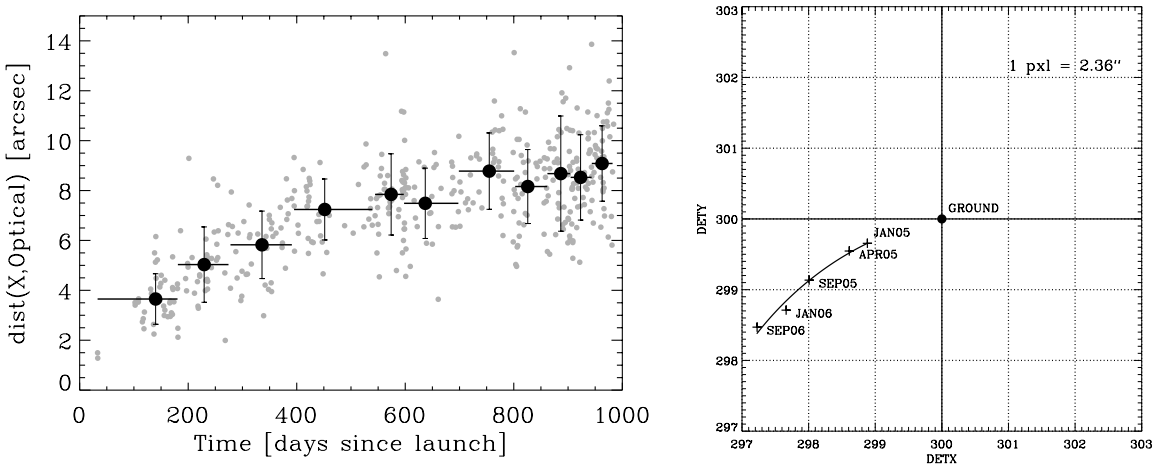

Figure 6. Left panel: the variation of the systematic error in the XRT position varied since the beginning of the mission due to the drift of the telescope and star tracker alignment. Grey dots are measurement of single observations; larger black circles are the mean values for each time interval. **Right panel:** such a variation can be mapped with good precision studying the boresight as a function of time.

The statistical error in the position determination depends on the instrumental PSF and on the counts of the source according to the simple formula $U_{stat} \propto R_{90}/\sqrt{counts}$, where U_{stat} is 90% accuracy error circle radius and R_{90} is the radius which contains 90% of the fluence. The XRT statistical positional accuracy has been extensively tested on–ground and verified in flight during the calibration phase with some ad hoc observations.[10] We empirically found that the statistical error at the 90% level of XRT position measurement is given by the formula $U_{stat}=R\times counts^{-0.48}$, with the parameter R=23 arcsec, in very good agreement with the expectations. It means that for a source with more than 144 counts, the statistical error is less than 2 arcsec. In addition to the statistical error, the XRT position uncertainty is also determined by the uncertainty in the satellite aspect solution. The nominal value of this uncertainty is 3 arcsec as reported in the calibration file swxposerr20010101v003.fits (CALDB version 20050916).

Moreover, we found that the the XRT positional accuracy is affected by a variation of the boresight with time. This effect is due to a drift between the XRT boresight and the satellite star tracker boresight, which causes a displacement of the detector system coordinate.

As shown in the left panel of Fig. 5, for a given time interval, we can quantify this misalignment studying the relationship between the spacecraft position angle (PA, also called roll angle) of the observations and the residuals in RA and DEC of the X–ray positions with respect to the correct positions of already known sources (note that RA residuals have been corrected by the factor cos (DEC), and represent the true separation in the sky). We describe this relation with a trigonometric function:[11]

$$\Delta(\mathrm{RA}) = \mathrm{A(t)}\sin(\mathrm{PA} + \delta(\mathrm{t})) \tag{4}$$

$$\Delta(\mathrm{DEC}) = \mathrm{A(t)}\cos(\mathrm{PA} + \delta(\mathrm{t})) \tag{5}$$

where A is the amplitude of the misalignment and the phase δ is its direction (Fig. 5). By studying the boresight calibration as a function of time, we can map the dependence of the boresight from time, A=A(t), δ(t), with good precision ($\sim$0.5 arsec). As shown in the left panel of Fig. 6 in the first 1.5 year of the mission the telescope boresight has changed by $\sim$ 8 arcsec from the initial position approximately along the same direction. This correction has been implemented in the standard calibration products since the Jan 2006 CALDB distribution.

4. BACKGROUND

The fraction of the XRT background which does not have cosmic origin is composed by two components: the electronic noise component, which is important at the lower energies, and a particle-induced component which dominates at the higher energies and is due to the interaction of particles in the orbital environment with the detectors and the structures that surround them. The failure of the thermo electric cooler power supply at the beginning of the mission forced the instrument to rely on the passive cooling provided by the radiator. As a consequence the CCD temperature varies in a range between -75° to -50°. The electronic background component is strongly dependent on the CCD temperature, with the number of hot and flickering pixels increasing with temperature[12] . Nevertheless, most of the electronic noise is concentrated in a few bad pixels and can be easily filtered out by the standard software. In correspondence of particular inclination angle of the telescope in respect to the Earth limb, XRT also suffers from an optical contamination due to a reflection of the albedo on the CCD, which is not filtered and acts as very low energy X–ray background. This produces flares on a few seconds time scale in the background light curve. In particular these happen towards the beginning and end of the observation segments. As illustrated in the left panel of Fig. 7, these flares can be eliminated by a simple σ clipping algorithm. Filtering out the flaring intervals reduces the background by a factor of 10-20% with time losses of the order of 2% (right panel of Fig. 7).

After the spatial (hot and flickering pixels) and timing (flares) filtering procedure, the 0.2-10.0 background count rate is 4.3×10^{-7} count s^{-1} $pixel^{-1}$ (7.6×10^{-8} count s^{-1} $arsec^{-1}$) with 46% in the 2–10 keV energy band (Fig. 8). We note that the XRT background is a factor 14 lower than the Chandra ACIS-I in the 0.3-10.0 energy band and a factor 22 lower in the 2–10 keV band.

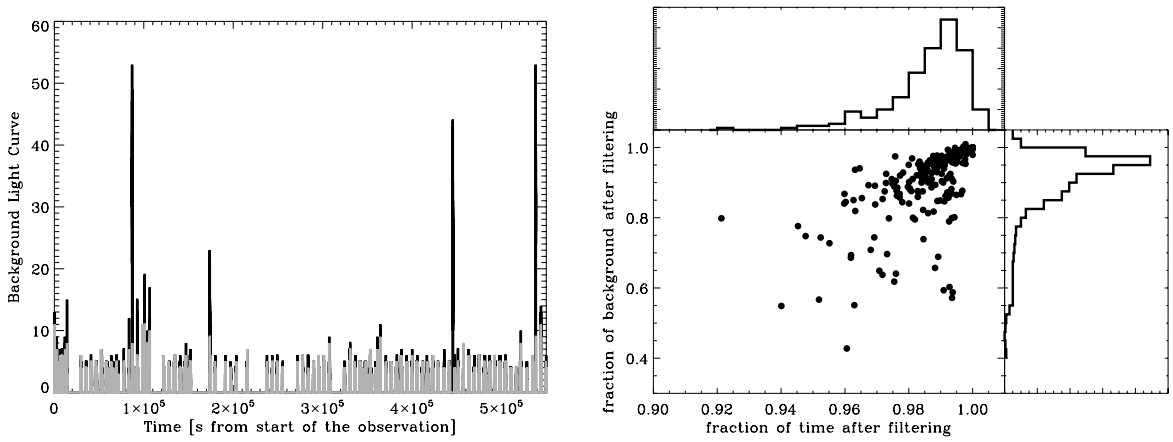

Figure 7. Left panel: As an example of very low energy flaring activity, we plot the case of the GRB070616 follow-up observation background light curve in the 0.2-10.0 keV energy band. The grey line is obtained applying a simple 3σ clipping filter on the light curve. **Right Panel:** For all the 221 observations, we plot the background reduction factor we obtain by filtering out high background episodes versus the fraction of the exposure we lose. Typically filtering out 2% of the exposure we can reduce the background level of 10–20%.

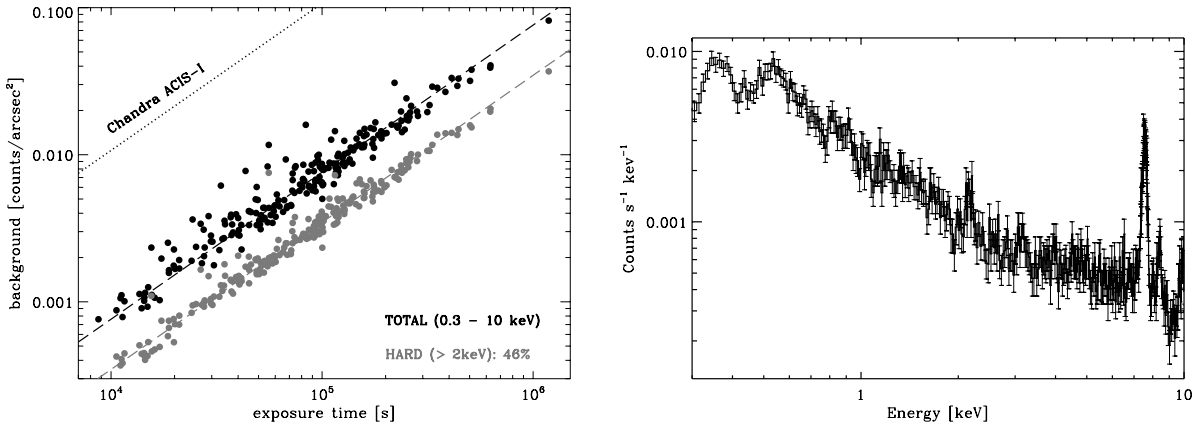

Figure 8. Left panel: The 0.2-10.0 count rate plotted against the exposure time for the 221 observations of the survey. **Right Panel:** The spectrum of the background as extracted by the 1.1 Ms follow-up observation of GRB060729. The two emission line are instrumental Nickel lines.

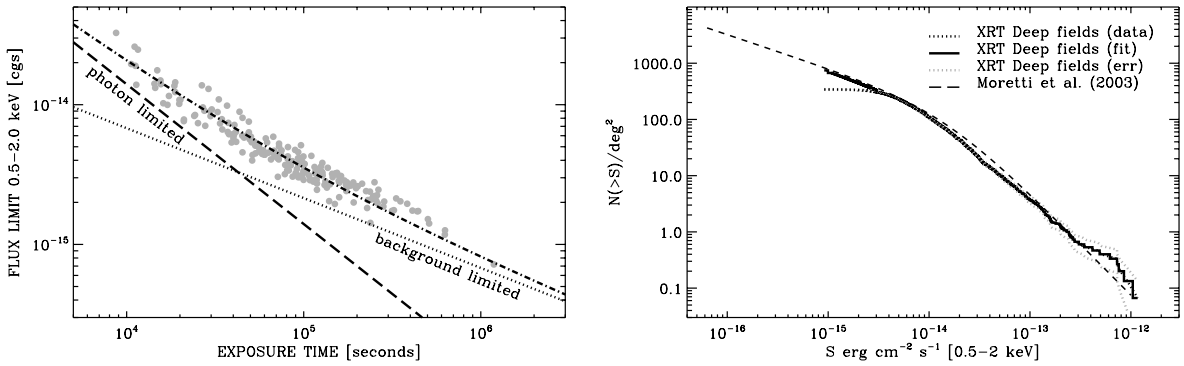

Figure 9. Left panel: The flux limits as a function of the exposure time. **Right Panel:** The Log N – Log S in the soft band compared with.[13]

5. FLUX LIMITS, SKY–COVERAGE AND LNLS OF THE SURVEY

In the ideal case of a uniform observation, given a value n_σ for the detection threshold in S/N ratio, the corresponding minimum detectable count rate (or flux limit) can be expressed by the following formula:

$$\mathrm{F_{lim}} = \frac{\mathrm{c_{min}}}{\mathrm{t_{exp}}} + \mathrm{n_{sig}} \frac{\sqrt{\mathrm{b}}\ \mathrm{d_{cell}}}{\sqrt{\mathrm{t_{exp}}}\ \mathrm{f_{cell}}}\ \mathrm{CF} \tag{6}$$

Here d_{cell} is the diameter of the detection cell; f_{cell} is the fraction of signal contained in the cell, b is the background count–rate, c_{min} is the minimum number of source counts needed for detection when the background is negligible and CF is the conversion factor between count rate and flux (which depends on the source spectrum and effective area curve). We note that the wavelet transform, by its very nature, maximizes the S/N ratio for each source by optimizing the choice of the detection cell dimension.

However, in the low S/N regime where the source flux is comparable with the background noise, the concept of flux limit becomes somehow arbitrary: sources with fluxes lower than the theoretical sensitivity limit can be detected with non–null probability. This is due to the fact that faint sources can be detected if they sit on a positive background fluctuation, while they are missed in the opposite case. For this reason, the concept of a sharp flux limit needs to be generalized with a statistical approach, in which the selection function describes the probability for a source with given properties to be detected. To evaluate the catalog *completeness* we performed extensive Monte Carlo simulations, embedding simulated sources (clusters and point–like) within realistic backgrounds and running the detection pipeline. In this way we can statistically define the flux limit, for each observation, as the flux for which we have the 50% detection probability. In the left panel of Fig. 9 we plot the flux limits versus the nominal exposure time of all the 221 observations and we compare it with Eq. (6) where we used the HEW and b as reported in the previous sections and d_{cell}=8, n_{sig}=3, c_{min}=7.

Joining the completeness function with the exposure maps (which also account for the vignetting) allows us to calculate the complete sky–coverage and compute the integral flux distribution (LNLS). In the right panel of Fig. 9 we show the Log N Log S plot for the soft band and extra-galactic observations (Galactic latitude > 20).

6. EXTENDED SOURCES

The main advantage in using the wavelet transform is the possibility of characterizing the detected sources on the basis of their extension and distinguishing the clusters of galaxies from point-like sources. Candidate sources are identified as local maxima above a given threshold in wavelet space; the preliminary product of the detection procedure is a source list with a rough determination of the position (the center of the pixel with higher coefficient), source size (the scale of the transform where the signal to noise is maximized) and total number of photons (the value of the maximum transform coefficient). Since the wavelet scale steps are discrete, the final

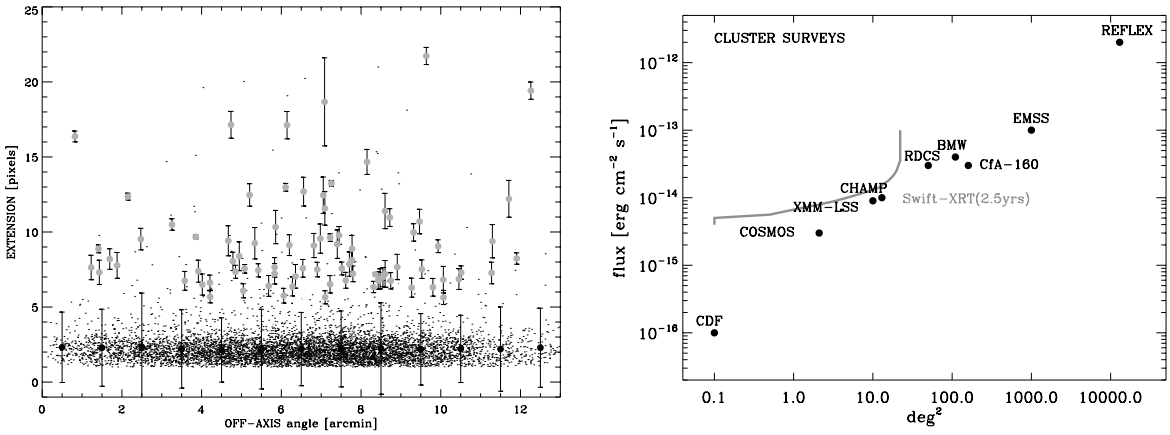

Figure 10. Left panel: The source width (W_{sou}) determined by the wavelet transform of the all 7159 sources is plotted (black dots) against the off–axis angle. Black circles are the mean instrumental extensions calcualted in different bin of off–axis angle. The grey circles are the 84 high significance (4σ) cluster candidates. **Right Panel:** A preliminary sky coverage for extended sources is compared to other recent cluster surveys.

catalogue parameters are a refinement of these values and are obtained through χ^2 minimization with respect to a Gaussian model in wavelet transform space. In particular the source extension parameter (W_{sou}) is defined as the width of the best-fitting Gaussian.

In order to distinguish extended from point-likesources, we split the W_{sou} distribution of source extensions into bins of 1 arcmin, as a function of the source off-axis angle, and within each bin, we applied a $\sigma-$clipping algorithm on the source extension: the mean and standard deviation in each bin are calculated and sources at more than $3\,\sigma$ above the mean value are discarded (Fig. 10, left panel). In this way we determine the mean instrumental extension $\langle W_p(\theta)\rangle$ and standard deviation $\sigma_p(\theta)$ of point-like source observed at different θ. This provides us with a threshold for defining truly extended sources. We define as candidate clusters all sources that lie above the $3\,\sigma_p(\theta)$ corridor, including their $2\,\sigma_{sou}$ error bar, i.e. those sources for which, at their observed off-axis angle θ, one has

$$W_{sou} - 2\sigma_{sou} > \langle W_p(\theta)\rangle + 3\,\sigma_p(\theta) \quad . \tag{7}$$

This combined requirement on the distance from the point-like source locus, and on the intrinsic error in the source extension, roughly corresponds to a $\sim 4\,\sigma$ confidence level for the extension classification. In our catalog we found 84 sources with absolute galactic latitude higher than 20 degrees meeting this criterion. After the construction of the catalog, one of the most critical points in order to infer the statistical properties of the sample is the computation of the survey volume or, equivalently, the survey sky-coverage. While this calculation for a point-like source catalog is quite straightforward, the one for an extended source catalog is much more complex. To this aim we are performing extensive Monte Carlo simulations of the entire detection and source characterization procedure under realistic conditions. The final product of these simulations will be the evaluation of the spurious contamination level for different detection thresholds and a family of different completeness functions and sky coverage curves for different source types and extensions. The whole detection pipeline and the simulation procedure has already been applied to the ROSAT HRI fields[14]; we followed the same steps, improving the evaluation and correction of the Eddington bias, by means of the effective recipe described by[15] . In the right panel of Fig. 10 we show the preliminary sky coverage curve, resulting from the first run of Monte Carlo simulations which we compare it with other cluster surveys.

REFERENCES

1. N. Gehrels, G. Chincarini, P. Giommi, and et al., "The Swift Gamma-Ray Burst Mission," *The Astrophysical Journal* **611**, pp. 1005–1020, 2004.

2. S. D. Barthelmy and et al., "Burst Alert Telescope (BAT) on the Swift MIDEX mission," *Space Science Review* **120**, p. in press, 2005.
3. D. N. Burrows and et al., "The Swift X-Ray Telescope," *Space Science Review* **120**, p. 165, 2005.
4. P. W. Roming and et al., "The Swift Ultra-Violet/Optical telescope," *Space Science Review* **120**, p. in press, 2005.
5. S. Campana and et al., "The Brera Multiscale Wavelet ROSAT HRI Source Catalog II: the Algorithm," *ApJ* **524**, p. 414, 1999.
6. S. Campana and et al., "The Brera Multiscale Wavelet ROSAT HRI Source Catalog II: Application to the HRI and first results," *ApJ* **524**, p. 423, 1999.
7. A. Moretti and et al., "The Brera Multiscale Wavelet Detection Algorithm Applied to the Chandra Deep Field South: Deeper and Deeper," *ApJ* **570**, p. 502, 2002.
8. P. Romano and et al., "The BMW-Chandra Serendipitous Source Catalogue," *Mem SAIT Suppl* **5**, p. 343, 2004.
9. A. Moretti, S. Campana, T. Mineo, and et al., "In-flight calibration of the Swift XRT point spread function," *Proc. SPIE* **5898**, pp. 360–370, 2005.
10. J. E. Hill, L. Angelini, D. C. Morris, and et al., "The unique observing capabilities of the Swift X-ray telescope," *Proc. SPIE* **5898**, p. 325, 2005.
11. A. Moretti and et al., "A refined position catalogue of the Swift XRT afterglows," *A&A* **448**, p. 9, 2006.
12. C. Pagani, D. C. Morris, J. Racusin, and et al., " Characterization and evolution of the Swift X-ray Telescope instrumental background," *Proc. SPIE* **6686**, p. in press, 2007.
13. A. Moretti and et al., "The resolved fraction of the Cosmic X–Ray Background," *ApJ* **588**, p. 696, 2003.
14. A. Moretti and et al., "The Brera Multi-scale Wavelet HRI Cluster Survey. I. Selection of the sample and number counts," *A&A* **428**, p. 21, 2004.
15. A. T. Kenter and S. Murray, "A New Technique for Determing the Number of X-Ray Sources per Flux Density Interval," *ApJ* **584**, p. 1016, 2003.